

# Sintering and concomitant crystallization of bioactive glasses

Poologasundarampillai, Gowsihan

DOI:

[10.1111/ijag.13477](https://doi.org/10.1111/ijag.13477)

License:

Creative Commons: Attribution (CC BY)

*Document Version*

Publisher's PDF, also known as Version of record

*Citation for published version (Harvard):*

Poologasundarampillai, G 2019, 'Sintering and concomitant crystallization of bioactive glasses', *International Journal of Applied Glass Science*, vol. 10, no. 4, pp. 449-462. <https://doi.org/10.1111/ijag.13477>

[Link to publication on Research at Birmingham portal](#)

## General rights

Unless a licence is specified above, all rights (including copyright and moral rights) in this document are retained by the authors and/or the copyright holders. The express permission of the copyright holder must be obtained for any use of this material other than for purposes permitted by law.

- Users may freely distribute the URL that is used to identify this publication.
- Users may download and/or print one copy of the publication from the University of Birmingham research portal for the purpose of private study or non-commercial research.
- User may use extracts from the document in line with the concept of 'fair dealing' under the Copyright, Designs and Patents Act 1988 (?)
- Users may not further distribute the material nor use it for the purposes of commercial gain.

Where a licence is displayed above, please note the terms and conditions of the licence govern your use of this document.

When citing, please reference the published version.

## Take down policy

While the University of Birmingham exercises care and attention in making items available there are rare occasions when an item has been uploaded in error or has been deemed to be commercially or otherwise sensitive.

If you believe that this is the case for this document, please contact [UBIRA@lists.bham.ac.uk](mailto:UBIRA@lists.bham.ac.uk) providing details and we will remove access to the work immediately and investigate.

## ORIGINAL ARTICLE

# Sintering and concomitant crystallization of bioactive glasses

Carsten Blaeß<sup>1</sup>  | Ralf Müller<sup>1</sup> | Gowsihan Poologasundarampillai<sup>2</sup>  | Delia S. Brauer<sup>3</sup> <sup>1</sup>Bundesanstalt für Materialforschung und -prüfung (BAM), Berlin, Germany<sup>2</sup>School of Dentistry, University of Birmingham, Birmingham, UK<sup>3</sup>Otto-Schott-Institut für Materialforschung, Friedrich-Schiller-Universität, Jena, Germany**Correspondence**

Delia S. Brauer, Otto-Schott-Institut für Materialforschung, Friedrich-Schiller-Universität, Fraunhoferstr. 6, 07743 Jena, Germany.

Email: delia.brauer@uni-jena.de

**Funding information**

EPSRC, Grant/Award Number: EP/M023877/1

**Abstract**

The sintering of bioactive glasses allows for the preparation of complex structures, such as three-dimensional porous scaffolds. Such 3D constructs are particularly interesting for clinical applications of bioactive glasses in bone regeneration, as the scaffolds can act as a guide for in-growing bone cells, allowing for good integration with existing and newly formed tissue while the scaffold slowly degrades. Owing to the pronounced tendency of many bioactive glasses to crystallize upon heat treatment, 3D scaffolds have not been much exploited commercially. Here, we investigate the influence of crystallization on the sintering behavior of several bioactive glasses. In a series of mixed-alkali glasses an increased CaO/alkali metal oxide ratio improved sintering compared to Bioglass 45S5, where dense sintering was inhibited. Addition of small amounts of calcium fluoride helped to keep melting and sintering temperatures low. Unlike glass 13-93, these new glasses crystallized during sintering but this did not prevent densification. Variation in bioactive glass particle size allowed for fine-tuning the microporosity resulting from the sintering process.

**KEYWORDS**

bioactive glass, crystallization, scaffolds, sintering

## 1 | INTRODUCTION

The reason for the clinical success of Bioglass 45S5,<sup>1</sup> which has been used clinically since the mid-1980s,<sup>2</sup> is its ability to degrade in aqueous solution, release calcium and phosphate ions, form a surface layer of hydroxycarbonate apatite and thus allow for the formation of an intimate bond to bone.<sup>1</sup> It has been described as a Class A bioactive material, bonding to both soft and hard tissue and degrading while being replaced by newly formed bone.<sup>3</sup> Owing to its inherent release of ions, such as silicon ions, it stimulates cell cycling and obviates the need for supplementation with growth factors.<sup>4,5</sup>

Clinical applications of bioactive glasses are mainly in bone regeneration and dental remineralization,<sup>6</sup> where they are used as either granules (ie, coarse particles) or fine powder. But one of the main advantages of glassy materials is their high-temperature

processing, which allows for shaping the material at elevated temperatures, to sinter coatings<sup>7,8</sup> or complex structures.<sup>9,10</sup> For bioactive glasses, however, this high-temperature processing has not yet resulted in clinical or commercial products.

One reason is that Bioglass 45S5, which has a highly disrupted silicate structure consisting of  $Q^2$  chains mostly with only small amounts (10%-15%) of  $Q^3$  branching units,<sup>11,12</sup> shows a pronounced tendency to undergo devitrification upon heat treatment. This makes it challenging to process the glass without crystallization occurring.<sup>13</sup> For bioactive glass applications, particularly in bone regeneration, the capacity to sinter complex, three-dimensional porous structures, so-called scaffolds, would be of great interest as this could broaden the field of clinical applications. Potential uses include porous implant materials, which simulate the structure of trabecular bone or templates in tissue engineering<sup>13</sup>. In

these applications, the porous scaffold acts as a 3D template, which ideally integrates well with existing tissue, allows for the ingrowth of cells, guides them to grow deep into the pores and stimulates them to form new bone but also allows for the growth of new blood vessels into this structure.

For this reason, this paper investigates the sintering behavior of Bioglass 45S5 and other bioactive glasses, to analyze how crystallization affects sintering and the resulting microstructure of the materials.

## 2 | EXPERIMENTAL PROCEDURE

### 2.1 | Glass and powder preparation

About 150 g batches of glass were prepared by a high-temperature melt-quench route as described previously.<sup>14</sup> Briefly, mixtures of SiO<sub>2</sub>, phosphates, carbonates, and CaF<sub>2</sub> were sintered together for 1 hour using a platinum crucible in an electric furnace at 1250°C, then melted for 1 hour at 1350°C. The melt was rapidly quenched into water, and the resulting glass frits were dried at 120°C. Glass monoliths were obtained by pouring the melt into brass moulds and annealing at the glass transition temperature before cooling to room temperature in the switched off furnace over night. Nominal glass compositions are shown in Table 1.

Glass powders were obtained from glass frits by crushing with a steel mortar and sieving into 32-42 μm, 56-63 μm, 125-140 μm, 180-200 μm, 300-315 μm, and 315-3150 μm fractions. From the 315-3150 μm fraction, powders were obtained by milling for 10 minutes in a planetary ball-mill (Pulverisette 5/2; Fritsch, Idar-Oberstein, Germany) using zirconia jars and milling balls. Milling was performed in isopropanol, and milled powders were dried in air at 55°C for half an hour. Glass powder particle size distribution was analyzed by light scattering (Mastersizer; Malvern, Worcestershire, UK) using a suspension of 10 mg glass powder dispersed in a 0.003 mol/L Na<sub>4</sub>P<sub>2</sub>O<sub>7</sub> solution. Table 2 shows the particle size distribution of the milled glass powder, referred to as "<32 μm" hereafter.

Glass powder compacts were obtained by uniaxially pressing 0.1 g glass powder (<32 μm) twice for 30 seconds each at 50 MPa using cylinders of 5 mm in diameter and height.

The relative density,  $\rho_{rel}$ , for all glass powder compacts was approximately 55%. Glass powders and powder compacts were stored in desiccators using P<sub>2</sub>O<sub>5</sub> or silica gel in an argon atmosphere in a low vacuum.

### 2.2 | Density and thermal properties

Glass density measurements were performed on glass monoliths using He gas displacement pycnometry (AccuPyc 1330; Micromeritics, Norcross, GA;  $\pm 0.01$  g cm<sup>-3</sup> accuracy). Results are presented in Table 1. Glass transition and crystallization temperatures were determined using differential thermal analysis, DTA (TAG24; Setaram, Caluire, France;  $\pm 5$  K accuracy) using 25 mg glass powder samples heated at 10 K min<sup>-1</sup> to 1300°C.

### 2.3 | Sintering

Sintering was studied on cylindrical powder compacts using a heating microscope (Leitz, Wetzlar, Germany). The compacts were placed on zirconia substrates (1.5 × 1 × 0.05 mm<sup>3</sup>; Ceramtec, Plochingen, Germany) and heated incrementally (30 K min<sup>-1</sup> to 300°C then 20 K min<sup>-1</sup> to 450°C and 10 K min<sup>-1</sup> above 450°C). Owing to slight variations in sample positioning and furnace temperature distribution, temperature accuracy was about  $\pm 10$  K. An integrated optical data acquisition system (Hesse Instruments, Osterode, Germany) recorded sample silhouette height ( $s_H$ ) and area ( $s_A$ ). Sintering shrinkage is presented as changes in  $s_A$  or alternatively as changes in relative density ( $\rho_{rel}$ ) calculated from  $s_A$ ,  $s_H$  and glass density,  $\rho$  (Table 1) and the sample mass,  $m$ , assuming ideal cylinder geometry and isotropic shrinkage according to:

$$\rho_{rel} \approx \frac{m}{\rho_G} \left( \frac{\pi}{4} \left( \frac{s_A}{s_H} \right)^2 s_H \right)^{-1} \quad (1)$$

Heating microscopy was also used to obtain sintered specimens for further analyses. Powder compacts were heated as described above but removed from the heating microscope at selected temperatures and quenched in air.

Glass	SiO <sub>2</sub>	CaO	Na <sub>2</sub> O	K <sub>2</sub> O	MgO	P <sub>2</sub> O <sub>3</sub>	CaF <sub>2</sub>	NC	$\rho$
13-93	54.6	22.1	6.0	7.9	7.7	1.7	—	2.6	2.65
45S5	46.1	26.9	24.4	—	—	2.6	—	2.1	2.72
ICIE16	49.4	36.3	6.6	6.6	—	1.1	—	2.1	2.72
F0	46.1	37.6	6.8	6.8	—	2.6	—	2.1	2.75
F1	45.7	37.1	6.8	6.8	—	2.6	1.0	2.1	2.76
F3	44.8	36.5	6.6	6.6	—	2.5	3.0	2.1	2.76
F8	42.4	34.6	6.3	6.3	—	2.4	8.0	2.1	2.77

**TABLE 1** Nominal glass composition (mol%), network connectivity, NC<sup>12</sup> and glass density,  $\rho$  (g cm<sup>-3</sup>;  $\pm 0.01$  g cm<sup>-3</sup>)

**TABLE 2** Particle size distribution data (in  $\mu\text{m}$ ) for milled glass powder (" $<32 \mu\text{m}$ ")

Glass	45S5	13-93	ICIE16	F0	F1	F3	F8
$D_{10}$	1.96	1.64	1.82	1.78	1.84	2.00	2.01
$D_{50}$	11.65	9.08	10.81	10.26	9.95	11.26	11.21
$D_{90}$	31.48	27.42	28.42	28.99	28.30	29.19	31.22

## 2.4 | Scanning electron microscopy

Fractured sintered powder compacts were analyzed using scanning electron microscopy, (SEM; XL30 ESEM-FEG, Philips, Eindhoven, the Netherlands) combined with energy dispersive X-ray (EDX, EDAX Inc.) analysis was used for these studies. EDX spectra were obtained using a 15 kV acceleration voltage at 0.3-0.5 torr  $\text{H}_2$  pressure.

## 2.5 | X-ray micro computed tomography

Micro computed tomography ( $\mu\text{CT}$ ) on all samples with the exception of F3 (particle size 180-200  $\mu\text{m}$ ) were performed at the I13-2 beamline of the Diamond Manchester Imaging Branchline at the Diamond Light Source synchrotron, Harwell, Didcot, UK.<sup>15,16</sup> Sintered powder compacts of approximately 1-2 mm in width were probed with polychromatic X-rays in the energy range of 8-30 keV and filtered with pyrolytic graphite (1.3 mm) and aluminium (3.2 mm) filters. The samples were rotated from 0 to 180° with an angular step size of 0.05°, collecting a total of 3601 projections (transmitted X-rays) with a 50 ms exposure. Transmitted X-rays were imaged using a 500  $\mu\text{m}$  thick  $\text{CdWO}_4$  scintillator-coupled sCMOS (2560x2160 pixels) detector (PCOpco.edge 5.5; PCO AG, Germany), positioned 10 mm from the sample. Scans were performed with a total magnification of 20 $\times$ , resulting in an effective isotropic pixel size of 0.33  $\mu\text{m}$ . Projections were reconstructed into tomograms using a filtered back projection algorithm.<sup>17-19</sup>

Sample F3 (180-200  $\mu\text{m}$ ) was scanned on a laboratory X-ray sourced CT (Skyscan 1172; Bruker, Belgium) using 80 kV voltage and 124  $\mu\text{A}$  current. Samples were rotated from 0° to 360° with an angular step size of 0.1° collecting a total of 3601 projections with a 900 ms exposure. Scans were performed with an overall isotropic voxel size of 1.5  $\mu\text{m}$ . Projections were reconstructed into tomograms using NRecon software (Bruker).

Tomograms were processed on Fiji.<sup>20</sup> First a 3D median filter was applied to remove noise. Glass and pores were segmented by applying a threshold using the histogram. Pore fraction was calculated from the threshold images. 3D rendering of the glasses were produced using the Volume Viewer plugin on Fiji.

## 2.6 | Infrared spectroscopy and X-ray diffraction experiments

Sintered powder compacts were crushed with a steel mortar and milled twice for 30 seconds in an agate ball mill (KM1;

Janetzki) for analysis by powder X-ray diffraction (XRD; D8 Advance; Bruker AXS, Karlsruhe, Germany;  $\text{Cu-K}\alpha$  radiation, scanning in 0.02° steps for 2 seconds in a 5 to 80° $2\theta$  range) and attenuated total reflection (ATR) Fourier-transform infrared spectroscopy (FTIR; Nicolet Avatar 370DTGS with art Orbit addition; Thermo Electron Corporation; 525-1700  $\text{cm}^{-1}$ ).

## 3 | RESULTS & DISCUSSION

Figure 1A,B illustrate changes in the silhouette area of powder compacts during heating microscopy studies, starting from relative densities of about 55% (compared to the density of glass monoliths). Results from heating microscopy and DTA summarized in Table 3 directly relate to the shrinkage during sintering and show dramatic differences between Bioglass 45S5 and the other glasses investigated here: While all other glasses reached a relative density of  $\geq 94\%$  at the end of shrinkage, Bioglass 45S5 reached about 67% only. This suggests that 45S5 did not sinter to compact specimens during the heating process but that a significant amount of porosity remained. Indeed, this poor sintering ability of 45S5 has been reported previously: Arstila and co-authors<sup>21</sup> noted that Bioglass 45S5 devitrified upon heating without any noticeable sintering before melting, and that cube-shaped monoliths of 45S5 crystallized upon heat treatment but retained their shape, in contrast to monoliths of other bioactive glass compositions which became more rounded.<sup>22</sup> This agrees well with results of SEM (Figure 2) and  $\mu\text{CT}$  studies here (Figure 3). Figure 2A shows SEM micrographs of powder compacts of 45S5 heated close to the end of shrinkage temperature,  $T_{\text{SE}}$  (Table 3). They show the presence of individual, non-rounded particles, seeming to be poorly sintered together. Even at higher temperatures (810°C, Figure 2B) the particle shape had not changed much. By contrast, individual particles could not be distinguished any longer for any of the other glasses heated close to the end of shrinkage temperature (Figure 2C-H), visible pores seemed small in number and size and often rounded in shape, confirming good sintering by viscous flow.  $\mu\text{CT}$  scans provided more detailed insight into changes in relative density and pore volume during sintering. The relative density of 45S5 changed from 55.7% (Figure 3A) near the onset of shrinkage temperature (580°C) to 65.6% (Figure 3B) at 710°C, well beyond the end of shrinkage temperature.

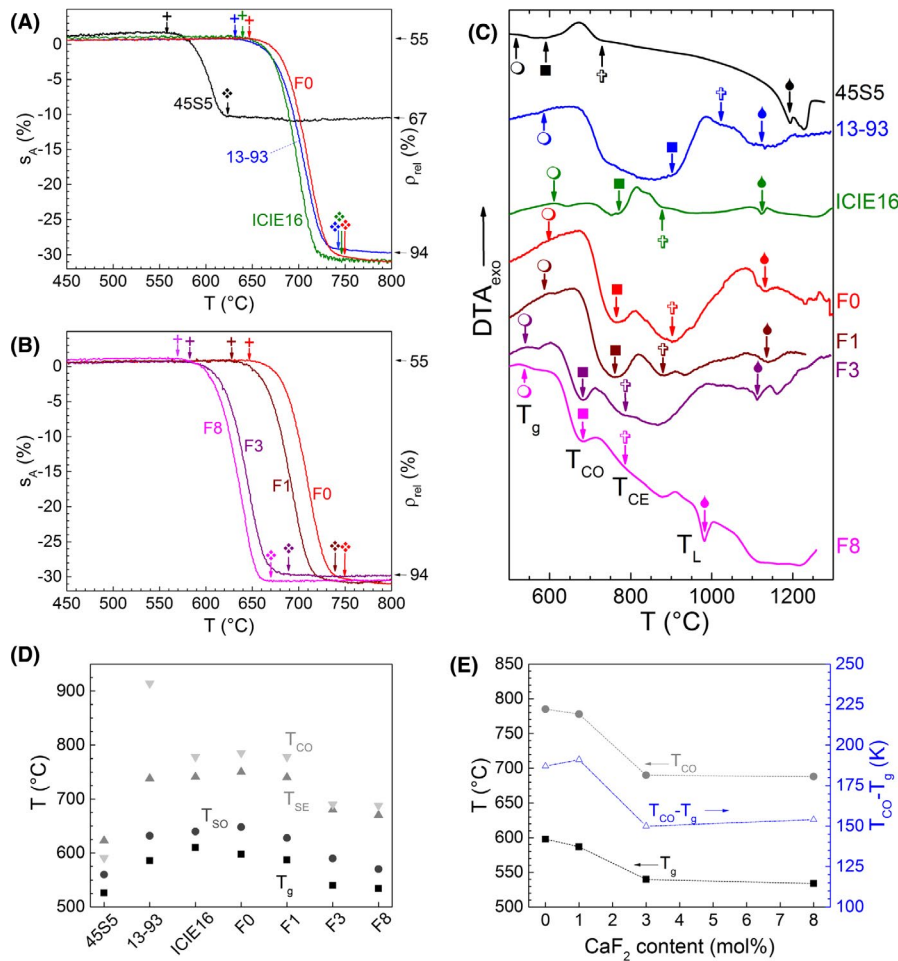


**FIGURE 1** (A,B) Relative silhouette area ( $s_A$ ) vs temperature during heating microscopy studies on glass powder compacts: (A) well-known glasses Bioglass 45S5, 13-93, ICIE16, and fluoride-free glass F0; (B) glasses F0 to F8. Relative density values ( $\rho_{rel}$ ) were calculated according to Equation 1. Arrows indicate shrinkage onset temperature,  $T_{SO}$  (+;  $ds_A/dT < -0.3\%/10\text{ K}$ ) and shrinkage end temperature,  $T_{SE}$  ( $\diamond$ ;  $ds_A/dT < 0.3\%/10\text{ K}$ ). (C) differential thermal analysis curves for glass powders  $<32\ \mu\text{m}$ . Arrows indicate glass transition temperatures ( $T_g$ ,  $\circ$ ), onset ( $T_{CO}$ ,  $\blacksquare$ ) and end temperature ( $T_{CE}$ ,  $\dagger$ ) of the first crystallization peak and the first detectable liquidus temperature ( $T_L$ ,  $\blacklozenge$ ). (D)  $T_g$ ,  $T_{SO}$ ,  $T_{SE}$ , and  $T_{CO}$  of the glasses. (E)  $T_g$  and  $T_{CO}$  of fluoride-containing glasses (left axis) and the processing window,  $T_{CO}-T_g$  (blue, right axis) vs their nominal  $\text{CaF}_2$  content (lines are visual guides only)

3D visualizations illustrate the significant amount of pore volume present, corresponding to 44.3% and 34.4%, respectively. For glass F3, the change in relative density was much more pronounced, densifying from 68.3% below the onset of shrinkage temperature ( $570^\circ\text{C}$ ) to 96.3% at  $720^\circ\text{C}$  (Figure 3C,D). 3D visualizations also highlighted the corresponding dramatic reduction in pore volume during sintering of glass F3 from 31.7% to 3.7%.

Comparing the results for the relative density of sintered powder compacts from heating microscopy (Figure 1A,B)

**TABLE 3** Characteristic process temperatures for glass powder compacts:  $T_g$  ( $\circ$  in Figure 1C),  $T_{SO}$  (+ in Figure 1A,B),  $T_{SE}$  ( $\diamond$  in Figure 1A,B),  $T_{CO}$  ( $\blacksquare$  in Figure 1C) (all in  $^\circ\text{C}$ ) and the temperature ranges  $T_{SO}-T_g$  and  $T_{CO}-T_{SE}$  (in K)

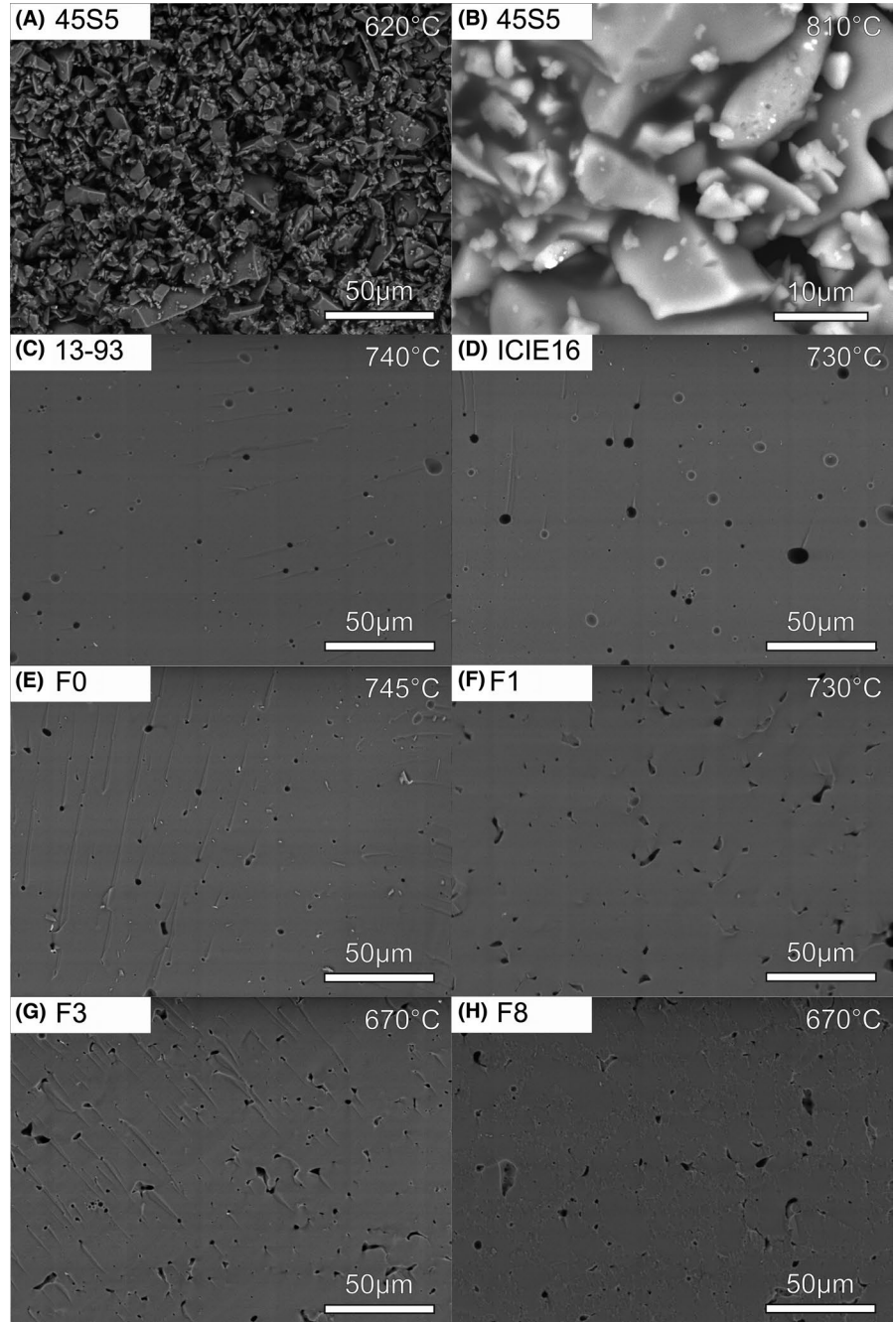
Glass	$T_g$	$T_{SO}$	$T_{SO}-T_g$	$T_{SE}$	$T_{CO}$	$T_{CO}-T_{SE}$
45S5	526	560	34	623	591	-32
13-93	586	632	46	738	914	176
ICIE16	610	640	30	741	778	37
F0	598	648	50	750	785	35
F1	587	628	41	740	778	38
F3	540	590	50	680	690	10
F8	534	570	36	670	688	18

and  $\mu\text{CT}$  (Figure 3), it is interesting to note that both methods give comparable results, although in heating microscopy relative densities were obtained from silhouette images rather than analyzing the entire three-dimensional structure as in  $\mu\text{CT}$ .

Differential thermal analysis curves (Figure 1C; results summarized in Table 3) of the glasses, with the exception of 45S5, showed the presence of marked shoulders above  $T_g$ , indicating the beginning of sintering. Heating microscopy allowed for precise measurement of the onset of shrinkage (Figure 1A,B; Table 3), which occurred about 30-50 K above  $T_g$ . The last column in Table 3 shows the temperature range between the end of sintering and the onset of crystallization,  $T_{CO}-T_{SE}$ , which relates to the sintering ability. For full densification, positive values are needed, and the amount of the positive deviation from zero provides a measure for the processing or sintering ability of a glass. Of the glasses studied here, only 45S5 showed a negative value for  $T_{CO}-T_{SE}$ , as the onset of crystallization actually occurred at lower temperature than the end of sintering. Figure 1D compares the trends of  $T_g$  vs  $T_{SO}$  as well as  $T_{SE}$  vs  $T_{CO}$ .  $T_g$  and  $T_{SO}$  followed the same trend for all glasses studied here: similar to the trend for the sintering shoulder in DTA curves,  $T_{SO}$  also was about 30-50 K above  $T_g$ .



**FIGURE 2** Fractured cross-sections of powder compacts prepared from milled glass powders after heating microscopy treatment to the temperature indicated followed by quenching in air



This should not come as a surprise, as for example, IUPAC defines  $T_g$  by the viscosity of the glass ( $10^{13}$  dPa s). The viscosity for the sintering of a porous body lies at approximately  $10^{8.8}$ - $10^8$  dPa s, that for the sintering of solid bodies at about  $10^6$  dPa s.<sup>23</sup> For most of the glasses studied here,  $T_{SE}$  and  $T_{CO}$  seemed to follow a similar trend, too. There are two notable exceptions, however: 45S5, where  $T_{CO}$  actually occurred at lower temperatures than the end of shrinkage, as mentioned above, and 13-93, where  $T_{CO}$  appeared at significantly higher temperatures than  $T_{SE}$ . The reason for comparable temperature ranges between  $T_{SE}$  and  $T_{CO}$  for most of the other glasses may be their similarity

in structure ( $NC = 2.1$ ) and composition. 13-93, however, has a much higher network connectivity (Table 1) than the other glasses studied here, owing to its larger  $SiO_2$ /modifier oxide ratio. Indeed, it has been noted before that bioactive glasses with a higher  $SiO_2$  content showed much improved processing.<sup>24</sup> The large temperature range between  $T_{SE}$  and  $T_{CO}$  for 13-93 is therefore likely to be caused mainly by its higher network connectivity, but other factors may play a role as well: MgO incorporation<sup>25</sup> and mixed alkali effect<sup>26</sup> both have been shown to widen the temperature range between  $T_g$  and crystallization. 13-93 has early been identified as a bioactive glass of good high temperature processing<sup>24</sup>

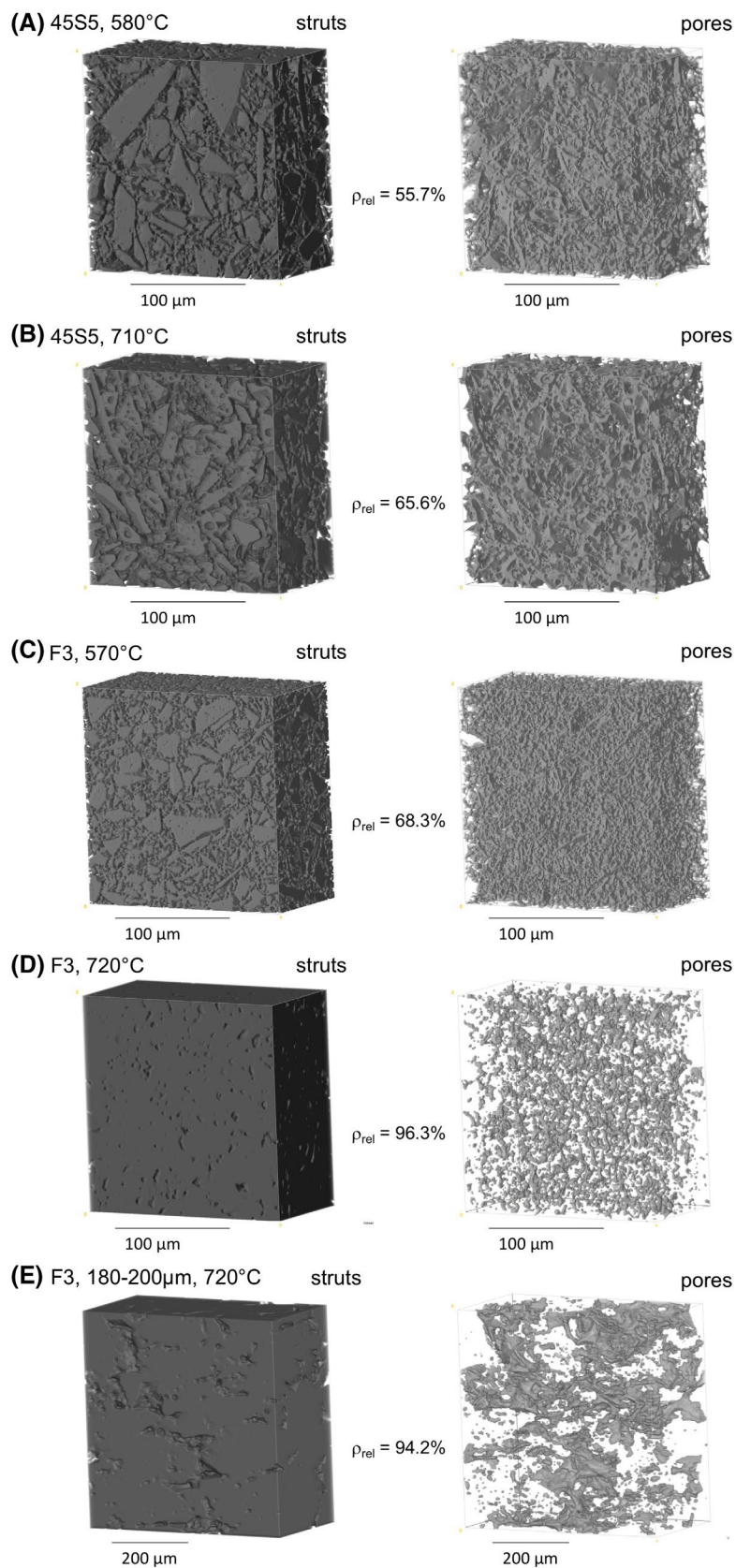


**FIGURE 3** 3D X-ray micro computed tomography images of powder compacts prepared from glass powders <32  $\mu\text{m}$  (A-D) or particles of the fraction 180-200  $\mu\text{m}$  (E) after heating microscopy treatment to the temperature indicated followed by quenching in air. Images on the left show the actual solid glass ("struts"), while the images on the right show the pore volume ("pores")

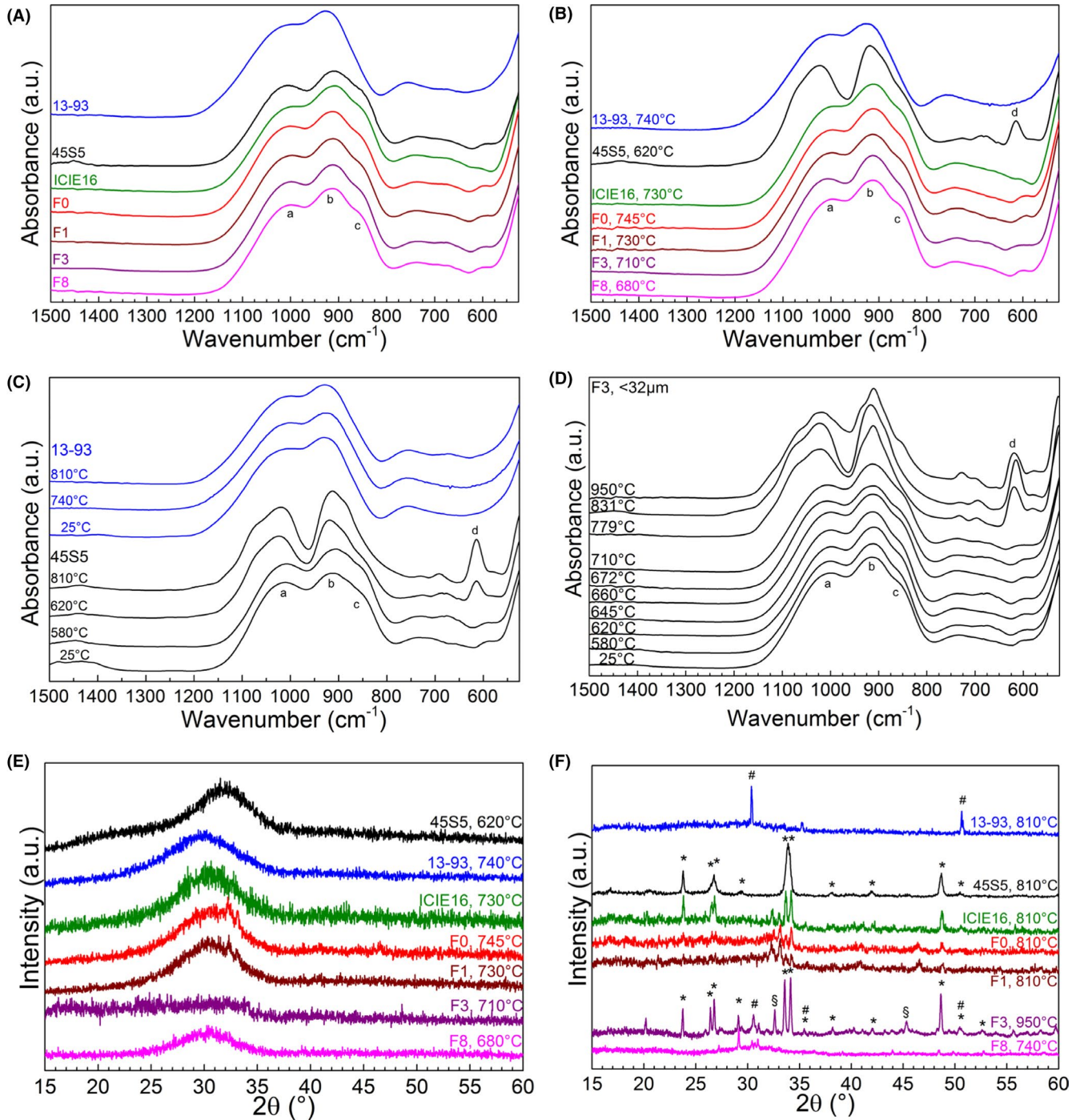


**FIGURE 4** Fourier-transform infrared spectra of the glass powders (A) before heat treatment, (B) of powder compacts treated in the heating microscope to  $T_{SE}$ , (C) powder compacts of 45S5 or 13-93 or (D) F3 treated in the heating microscope to various temperatures followed by quenching in air. Bands labelled a to d are discussed in the text. X-ray diffraction patterns of powder compacts treated in the heating microscope to (E)  $T_{SE}$  or (F) higher temperatures as indicated, followed by quenching in air. Crystal phases are #wollastonite,  $\text{CaSiO}_3$ ; \* $\text{Na}_2\text{CaSi}_2\text{O}_6$  (or  $\text{Na}_2\text{Ca}_2\text{Si}_3\text{O}_9$ ), and  $\text{S}$ silicorhenanite,  $\text{Na}_2\text{Ca}_4(\text{PO}_4)_2\text{SiO}_4$

and comparably low crystallization tendency.<sup>27</sup> It has been used successfully for the sintering of porous scaffolds by varying methods such as foam replication technique<sup>28</sup> or unidirectional freezing<sup>29</sup> or the preparation of glass fibres by drawing from pre-forms,<sup>21</sup> from the melt<sup>21</sup> or by melt spinning.<sup>30</sup> 13-93 also shows bone bonding in vivo.<sup>31,32</sup>

As Bioglass 45S5 was the first bioactive glass developed and also has been used clinically with great success, several studies have looked into its sintering and crystallization behavior, mostly with regard to the preparation of scaffolds. Bretcanu et al<sup>33</sup> investigated the sintering behavior of fine powder (mean particle size < 5  $\mu\text{m}$ ) of



commercial 45S5 samples using heating microscopy and found that in addition to a sintering range between 500 and 600°C (approximately the same temperature range as the one investigated in the present study) a second sintering range could be detected at higher temperature between 850 and 1000°C. According to our DTA results presented here, this second sintering range is still below the liquidus temperature. Based on these results, Bretcanu et al chose 1050°C as their optimum sintering temperature. The authors identified a sodium calcium silicate,  $\text{Na}_2\text{Ca}_2\text{Si}_3\text{O}_9$ , crystal phase, irrespective of the temperature studied. The authors also detected silicorhenanite,  $\text{Na}_2\text{Ca}_4(\text{PO}_4)_2\text{SiO}_4$ , as a minor, secondary phase.<sup>33</sup> Further crystallization studies on 45S5 indicated a variation in the crystallization mechanism with particle size, that is, with coarse or fine powder, and the authors suggested that the crystallization mechanism might be more complex than a simple nucleation and growth process and possibly involved phase separation.<sup>34</sup> Later studies confirmed that the nature of phase separation indeed had an influence on 45S5 crystallization and that this effect was much less pronounced for powder than for bulk samples.<sup>35</sup>

Densification of porous glass bodies during heat treatment is driven by the particles' surface energy, and the surface area is minimized through viscous flow.<sup>36</sup> However, if crystallization occurs at the same time, particularly surface crystallization, viscous flow is affected as the crystallized surface does not flow and, as a result, the sintering process is slowed down or inhibited.<sup>36</sup> If crystallization produces a residual glassy phase of which the composition (and thus the viscosity) differs from that of the original glass, viscous flow sintering may be affected even in the absence of crystalline surface layers.<sup>36</sup> Considering the narrow processing window of Bioglass 45S5,<sup>37,38</sup> it is likely that surface crystallization is the reason for its poor densification during sintering, and, indeed, this has been reported earlier.<sup>33,39</sup> Uniaxial load applied during sintering has been shown to help to achieve full densification for 45S5, and it also helped to reduce the sintering temperature from 1050°C to 610°C.<sup>40</sup>

Crystallization can be followed by structural analyses such as vibrational spectroscopy or XRD. FTIR spectra of the untreated glasses (Figure 4A) showed the typical shape for bioactive glasses, characterized by a bridging oxygen (BO) band at about 1000  $\text{cm}^{-1}$  (band a) and two non-bridging oxygen (NBO) bands at about 900 and 850  $\text{cm}^{-1}$  (b and c). For 13-93, the spectrum looked slightly different, as the NBO band (c) at 850  $\text{cm}^{-1}$  was absent, owing to the lower modifier content and higher network connectivity (Table 1) compared to the other glasses studied here. FTIR spectra of powder compacts heat-treated to  $T_{\text{SE}}$  (Figure 4B) showed changes for 45S5 only. The shape of bands b and c in the BO and NBO region had changed markedly, with features having become a lot more distinct, suggesting an increased structural order. An

additional band (d) had appeared at about 600  $\text{cm}^{-1}$ , possibly related to phosphate species.<sup>41</sup> Interestingly, the corresponding XRD pattern of the same 45S5 sample (Figure 4E) did not show any indication for the presence of crystalline phases, with only an amorphous halo being visible. A possible explanation for this difference may be that ATR-FTIR analyses are better suited to detect surface features than XRD analyses are. Once 45S5 was treated to higher temperatures (810°C, Figure 4F), the amorphous halo had disappeared and reflections indicated the presence of a crystalline phase, which in the literature has been identified as either  $\text{Na}_2\text{CaSi}_2\text{O}_6$ ,<sup>38,42</sup> or as  $\text{Na}_2\text{Ca}_2\text{Si}_3\text{O}_9$ .<sup>33,39,43</sup> Both phases show very similar diffraction patterns, are known to form solid-solutions within the series  $\text{Na}_{6-2x}\text{Ca}_{c+x}\text{Si}_6\text{O}_{18}$  ( $0 \leq x \leq 1$ ) and are similar to the mineral combeite.<sup>44,45</sup> While the FTIR spectra of glasses F0 and F1 showed no indication of crystallization, two low-intensity reflections were present at about 32 and 33° $2\theta$  in the XRD patterns of these samples treated to  $T_{\text{SE}}$  (Figure 4E). In the patterns of these glasses treated at higher temperatures, the same reflections seemed to be present, but had not increased in intensity. Instead, high intensity reflections corresponding to  $\text{Na}_2\text{CaSi}_2\text{O}_6$  (or  $\text{Na}_2\text{Ca}_2\text{Si}_3\text{O}_9$ ) were present. The fact that the intensity of the reflections at 32 and 33° $2\theta$  did not change with heat treatment is interesting. As they correspond to the two highest intensity peaks in the diffraction pattern of apatite, and as it has been shown that bioactive glass powders can form apatite not only when immersed in aqueous solution but also by reactions with atmospheric humidity,<sup>46</sup> we cannot exclude that the same has happened here.

Particularly interesting is the difference in the sintering behavior of glasses 45S5 and F0, which are actually quite similar in composition. The two glasses share the same  $\text{SiO}_2$  and  $\text{P}_2\text{O}_5$  content and the same network connectivity. However, F0 has a larger CaO/alkali metal oxide ratio and also contains two types of alkali metal cations, thereby making use of the mixed alkali effect, which is known to reduce the crystallization tendency.<sup>26</sup> Wallace et al have investigated the effect of the  $\text{Na}_2\text{O}/\text{CaO}$  ratio on thermal properties including  $T_g$  and crystallization temperature.<sup>47</sup> Although unfortunately their DSC traces are not shown and only crystallization peak temperatures (rather than crystallization onset) are given, results suggest a trend to a smaller processing window, that is, temperature range between  $T_g$  and crystallization, with a larger  $\text{Na}_2\text{O}/\text{CaO}$  ratio. Other studies confirmed this by showing that bioactive glasses with large alkali metal oxide contents not only showed low  $T_g$  values but also low crystallization temperatures.<sup>21,48,49</sup> More importantly, these studies highlighted that not only crystallization per se, but particularly the type of crystal phases being formed played a major role with regard to the processing behavior of bioactive glasses. The glasses in those studies could be grouped according to the main crystal phase being formed during heat treatment, as they either crystallized to sodium calcium silicates (NCS, including  $\text{Na}_2\text{Ca}_2\text{Si}_3\text{O}_9$ ) or to

calcium silicate (wollastonite,  $\text{CaSiO}_3$ , CS). Glasses crystallizing to NCS (e.g. 45S5) showed poor processing properties and crystallized about 100 K above  $T_g$ .<sup>49</sup> By contrast, glasses crystallizing to CS (e.g. 13-93), showed much improved processing, crystallized at significantly higher temperatures and were particularly suitable for processes which involved a large surface area to volume ratio, such as sintering of powders. The crystal phases formed were controlled *via* the glass composition, particularly the  $\text{Na}_2\text{O}/\text{CaO}$  ratio, with a large ratio favoring crystallization of NCS. Studies by Vedel et al<sup>49</sup> found a correlation also between the crystal phases being formed upon heat treatment (NCS vs CS) and their apatite-forming ability in simulated body fluid (SBF). Glasses which crystallized to NCS upon heat treatment tended to form apatite faster, resulting in thicker layers, while glasses from the CS group tended to be slower in forming apatite.

In the present study, however, there seemed to be no correlation between glass processing and crystal phases formed. Except for glass 13-93, all glasses showed NCS as the main crystal phase appearing during heat treatment, despite significant differences in their sintering. With increasing  $\text{CaF}_2$  content, that is, with increasing  $\text{Ca}/\text{Na}$  ratio, wollastonite appeared as a second crystalline phase. This, however, did not coincide with a larger temperature range between  $T_{\text{SE}}$  and  $T_{\text{CO}}$  or between  $T_g$  and  $T_{\text{CO}}$ , and thus does not seem to indicate improved processing here. Although glass ICIE16 is known to show significantly better processing at higher temperatures<sup>50,51</sup> than 45S5 and also has a much higher  $\text{CaO}$  content, both seemed to crystallize to the same phase (Figure 4F), possibly because of their similarity in network connectivity.<sup>52</sup> The only difference was that the reflections were better resolved for glass ICIE16 (as well as for glass F0-F8), while for example the two peaks at  $33.5$  and  $34.5^\circ 2\theta$  overlapped for 45S5. The reason for this lack of resolution may be the higher

$\text{Na}_2\text{O}$  content of 45S5 together with the fact that in this region formation of solid solutions occurs readily.<sup>44,45,53</sup> This may have caused peak broadening for 45S5, an effect which has been observed previously for similar glass compositions.<sup>54</sup> The main difference between glasses ICIE16 and F0 is their phosphate content. While an increase in phosphate content has been shown to increase the tendency of a bioactive glass to crystallize,<sup>55</sup> no such effect was observed here, probably because the overall  $\text{P}_2\text{O}_5$  contents of both glasses are still low. This difference in phosphate content of these two glasses has, however, been shown to affect the rate at which apatite formed during *in vitro* immersion experiments.<sup>14</sup>

Fluoride has been shown to affect the thermal properties of bioactive glasses,<sup>14,37,43,54</sup> and as a result it also affects the sintering behavior here: with increasing  $\text{CaF}_2$  content, the onset of shrinkage moved to lower temperatures. However, the trend was not linear. Instead, temperature differences between the sintering onset temperatures of F0 vs F1 or F3 vs F8 were very small, while there was a large gap between F1 and F3 (Figure 1B). The same trend was obvious for  $T_g$  (Figure 1E), which is in contrast to earlier studies on the same glass compositions (but different batches),<sup>14,37</sup> which showed  $T_g$  to decrease linearly with increasing  $\text{CaF}_2$  content. This difference may possibly be explained by slight variations in the actual  $\text{CaF}_2$  content of the glasses, as fluoride losses are well-known to occur during melting and are difficult to control.<sup>56</sup> The decrease in  $T_g$ , and thus in the onset of shrinkage, can be explained by the structural role of fluoride in these glasses. Fluoride has been shown to complex modifier ions such as calcium and sodium,<sup>54,57,58</sup> and to form fluoride- and modifier-rich regions or clusters.<sup>42,59</sup> The fluoride and modifier ions in these regions can be expected to show a high mobility at elevated temperatures, and they thus lower the overall  $T_g$ , but also crystallize easily. As a result, for glasses

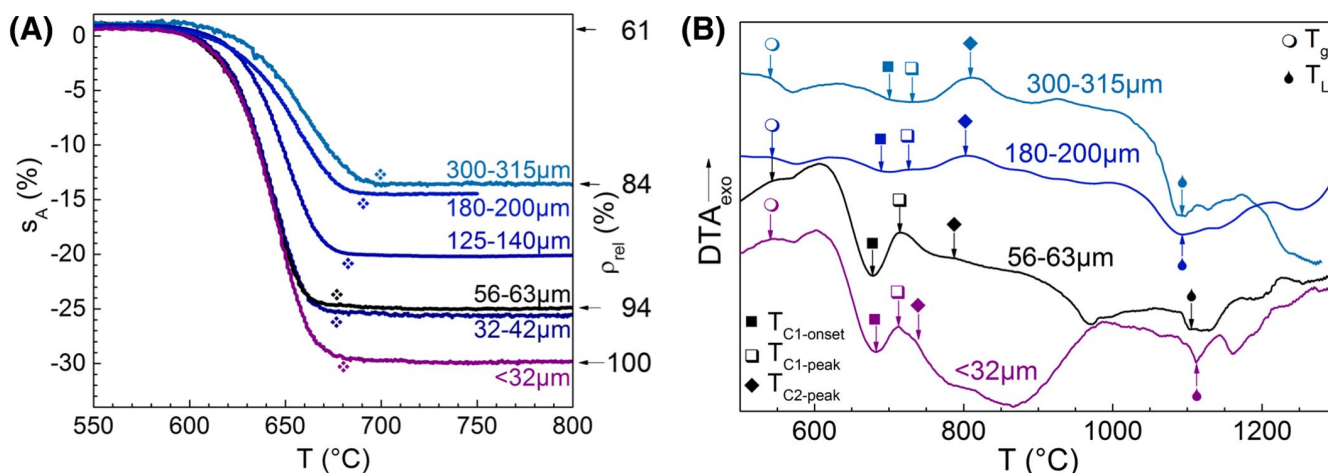


**FIGURE 5** (A) Heating microscopy and (B) differential thermal analysis (DTA) results for different particle size fractions of glass F3. (A) Relative density values ( $\rho_{\text{rel}}$ ) were calculated according to Equation 1. Shrinkage end temperature,  $T_{\text{SE}}$ , is indicated (❖;  $ds_A/dT < 0.3\%/10$  K). (B) Arrows indicate glass transition temperatures ( $T_g$ , ○), onset ( $T_{\text{CO}}$ , ■) of the first crystallization peak, crystallization peak temperatures (□, ◆) and the first detectable liquidus temperature ( $T_L$ , ●)

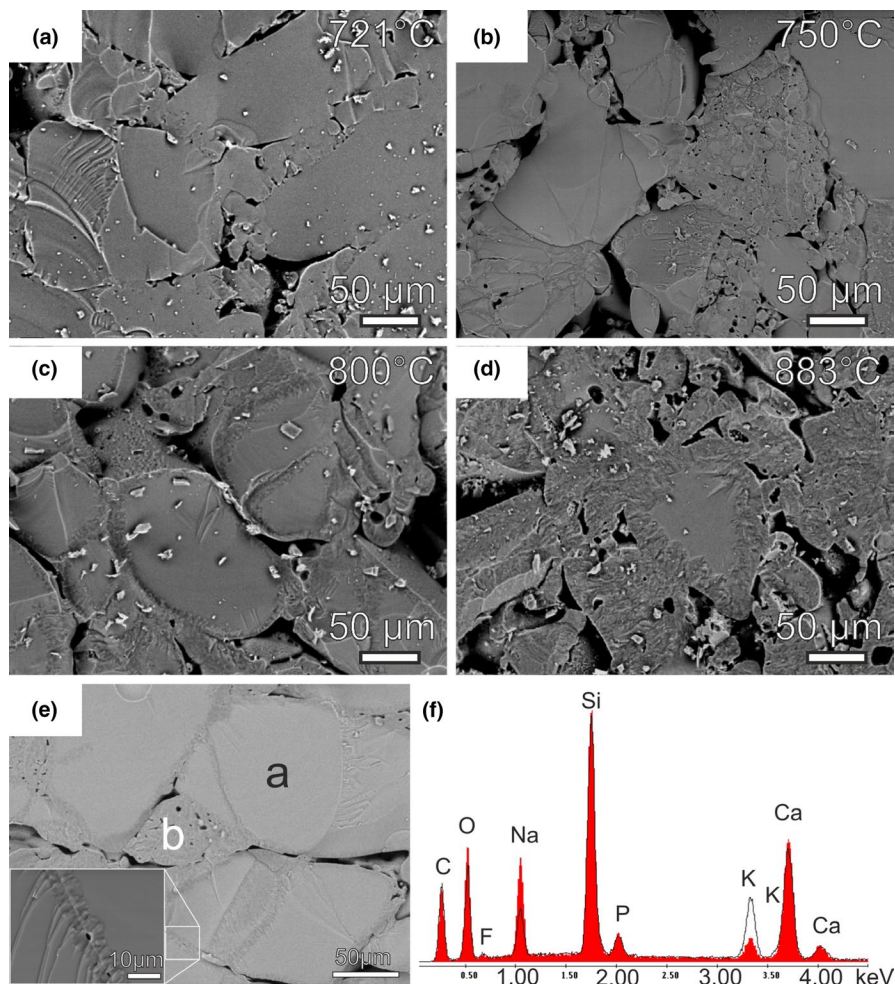


**FIGURE 6** (A-E) Scanning electron microscopy micrographs of fractured cross sections of powder compacts of glass F3 (particle size range 180-200 μm) and (F) results of energy dispersive X-ray measurement on (a) a glass grain and (b) a crystallized region as indicated in (E)

F0-F8 the temperature range between  $T_{SE}$  and  $T_{CO}$  becomes smaller with increasing  $CaF_2$  content (Figure 1d), indicating the influence of even small compositional variation on the sintering behavior.

As glass F3 nearly fully densified during sintering of glass powders (<32 μm), this composition was chosen for further analyses. Figure 5A shows the shrinkage for different particle size fractions of glass F3 during heating microscopy. Green density of all samples was  $61 \pm 3\%$ . Results illustrate that the shrinkage, and thus the densification during sintering, decreased with increasing particle size, changing from nearly full densification ( $\rho_{rel} \geq 94\%$ ; particle size <32 μm) to a relative density of 84% (300-315 μm). This is expected based on classical models of sintering kinetics,<sup>60</sup> and it has previously been observed for bioactive glasses.<sup>61</sup> As a result, sintered bodies were more porous if they had been prepared from larger particles, with heating microscopy giving a porosity of about 15% for particles in the 180-200 μm size range, compared to virtually no porosity for particles sieved to <32 μm (Figure 5A). Results from μCT scans differ less, however (Figure 3D,E; F3) showing 5.8% porosity for bodies sintered from particles in the 180-200 μm size range and 3.7% porosity for those sintered from particles sieved to <32 μm. The

corresponding DTA curves (Figure 5B) show that the pronounced sintering shoulder between  $T_g$  and crystallization disappeared with increasing particle size. It is interesting to note that the temperature of maximum densification ( $T_{SE}$  indicated in Figure 5A) clearly correlates with the onset of the first crystallization peak observed in DTA curves for particle size fractions <32, 56-63 and 180-200 μm. This, again, indicates that sintering is strongly affected by beginning crystallization. It is known that viscous sintering can be fully impeded by the presence of a compact crystal surface layer, regardless of its volume fraction.<sup>62,63</sup> The trend for onset temperature and peak height observed in Figure 5B suggests that crystallization affected sintering of the largest particle size fraction (300-315 μm) as well, even though the first crystallization peak was much weaker in intensity and a second broad crystallization peak appeared at higher temperature.

Figure 6A-D show SEM micrographs of fractured cross-sections of sintered F3 powder compacts (180-200 μm) heated to various temperatures above their shrinkage end temperature (690°C). At 721°C (Figure 6A), rounded particles revealed progressive viscous flow and sintering. The presence of porosity, which had been quantified as about 15% (based on density measurements, Figure 5A) or 5.8%



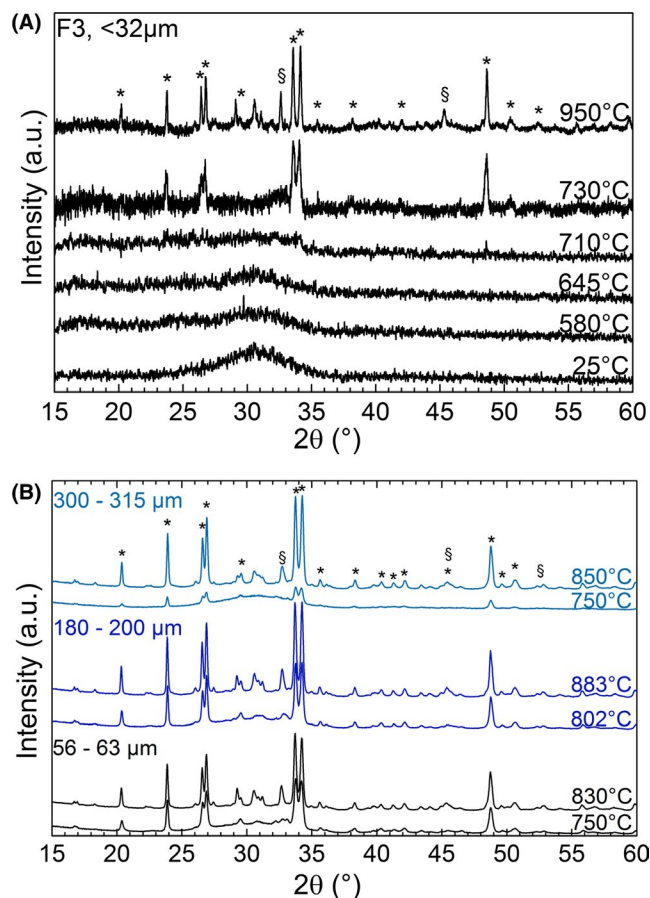


**FIGURE 7** X-ray diffraction patterns of (A) F3 powder compacts (<32  $\mu\text{m}$ ) treated in the heating microscope to different temperatures and of (B) F3 for grain size fractions 56–63  $\mu\text{m}$ , 180–200  $\mu\text{m}$  or 300–315  $\mu\text{m}$  heated to temperatures of the 1st and 2nd differential thermal analysis crystallization peak. Crystal phases are \* $\text{Na}_2\text{CaSi}_2\text{O}_6$  (or  $\text{Na}_2\text{Ca}_2\text{Si}_3\text{O}_9$ ) and §silicorhenanite,  $\text{Na}_2\text{Ca}_4(\text{PO}_4)_2\text{SiO}_4$

(based on  $\mu\text{CT}$  on a separate specimen undergoing an identical heat treatment; Figure 3E), and the irregular shape of the pores, however, clearly indicate that sintering was inhibited compared to powder compacts of smaller particles (Figures 2G and 3D,E), although the micrographs showed no apparent presence of crystal phases. Even a very thin crystalline layer could possibly prevent shrinkage, though, and some small (micrometre-size range; Figure 6B) heterogeneities were indeed apparent from 750°C. Fully sintered particle agglomerates appeared, with former grain boundaries being visible as thin crystalline ("surface") layers. When heating to temperatures  $\geq 800^\circ\text{C}$  (Figure 6C,D), that is, above the second DTA crystallization peak, pronounced surface crystallization and a significant crystalline volume fraction became evident. Figure 6E shows the sample treated to 750°C in more detail. The non-crystalline parts of the particles are shown as homogeneous light grey areas (a), while crystalline parts can be distinguished by their darker shade (b).

The inset clearly confirms the presence of a crystalline surface layer, about 5  $\mu\text{m}$  in thickness, on the particles. EDX analyses (Figure 6F) in region b show an increased sodium content and reduced potassium content compared to the non-crystalline parts (a).

X-ray diffraction patterns (Figure 7A) of F3 glass powder compacts (<32  $\mu\text{m}$ ) showed a pronounced amorphous halo at about 28 to 33 $^\circ 2\theta$  for the non-heat treated sample. With increasing temperature, this amorphous halo became less pronounced, but until 710°C no crystalline reflections were detected. Similarly, FTIR spectra (Figure 4D) of heat-treated F3 did not show any changes up to that temperature, despite the crystallization onset temperature for this particle size fraction having been found to be 690°C by DTA. This discrepancy in temperature may originate, however, from two different instruments having been used for thermal analysis (DTA) and heat treatment/sintering (heating microscope). At higher temperatures, FTIR spectra started showing a sharpening of the NBO silicate band (b) at 914  $\text{cm}^{-1}$  and, to some extent, the BO band (a) at 1020  $\text{cm}^{-1}$  as well as the appearance of a pronounced phosphate band (d) at 623  $\text{cm}^{-1}$ . From 730°C, high intensity reflections in XRD patterns indicated the presence of  $\text{Na}_2\text{CaSi}_2\text{O}_6$  (or  $\text{Na}_2\text{Ca}_2\text{Si}_3\text{O}_9$ ) (Figure 7A). The first crystallization peak in DTA traces (at 720°C) can therefore be attributed to formation of one of these phases (or possibly a mixture). When heating to 950°C, that is, well above the weak DTA shoulder at 740°C and the weak DTA peak at 820°C (Figure 5B), additional reflections appeared. One of them was identified as the apatite-like silicorhenanite,  $\text{Na}_2\text{Ca}_4(\text{PO}_4)_2\text{SiO}_4$ , which has previously been shown to crystallize from bioactive glasses.<sup>33,64,65</sup> The remaining, minor phase (or phases) with main reflections appearing in the range of 30 to 32 $^\circ 2\theta$ , could not be identified unambiguously, but considering the appearance of a phosphate band in FTIR spectra may well relate to an orthophosphate, which also has been reported previously.<sup>42</sup> The detailed assignment of these secondary crystal phases, which probably had a negligible influence only on the sintering in the temperature range studied here, will require further analyses and is beyond the scope of the present study.

X-ray diffraction patterns of sintered powder compacts obtained from coarse particle size fractions (56–63, 180–200, or 300–315  $\mu\text{m}$ ) heat-treated to two different temperatures (Figure 7B) also showed  $\text{Na}_2\text{CaSi}_2\text{O}_6$  (or  $\text{Na}_2\text{Ca}_2\text{Si}_3\text{O}_9$ ) as the main crystal phase. For particle size 300–315  $\mu\text{m}$ , the reflections were rather weak at 750°C, as the first DTA crystallization peak was also weak (Figure 5B), but reflections increased in intensity for 850°C, i.e. above the second DTA crystallization peak. This finding indicates that the first and second DTA peaks did not correspond to different crystal phases but could be connected to different modes of overall crystallization of  $\text{Na}_2\text{CaSi}_2\text{O}_6$  (or  $\text{Na}_2\text{Ca}_2\text{Si}_3\text{O}_9$ ). Such behavior has been observed for strong surface nucleation, where a thin, dense crystalline surface layer (as seen in Figure 6)



was formed at early stages, causing a first DTA peak, while its volume fraction was still small for coarse glass particles. Once the surface is completely coated by a crystalline layer, lateral crystal growth is impeded and crystals grow towards the bulk instead (as seen in Figure 6D, 883°C), which sometimes causes a second DTA peak.<sup>62,66–68</sup> The XRD patterns in Figure 7B also show the presence of minor phases, for example, silicorhenanite,  $\text{Na}_2\text{Ca}_4(\text{PO}_4)_2\text{SiO}_4$ , similar to those observed above for smaller particle sizes.

Sintering studies here were performed on compact pellets, and further studies are necessary to investigate the preparation of highly porous 3D scaffolds. Depending on the method chosen for scaffold preparation, for example, foam replication technique,<sup>28</sup> gel-cast foaming<sup>50</sup> or additive manufacturing,<sup>69</sup> too low a viscosity of the glass during sintering may possibly result in the collapse of the pore structure. Here, beginning crystallization might provide a stabilizing effect and may thus be advantageous for certain bioactive glass compositions.

## 4 | CONCLUSIONS

Taken together our results show that while crystallization inhibits complete sintering of Bioglass 45S5 at temperatures around 600°C, crystallization does not necessarily prevent the dense sintering of bioactive glasses, depending on the glass composition. Here we demonstrate that using glasses with a large alkaline earth to alkali metal oxide ratio, mixed alkali compositions as well as a low fluoride content, compositions can be obtained which sinter by viscous flow to nearly fully densified specimens. This happens even if the glass network connectivity remains the same as for Bioglass 45S5. Only with increasing particle size sintering is increasingly inhibited by surface crystallization of  $\text{Na}_2\text{CaSi}_2\text{O}_6$  (or  $\text{Na}_2\text{Ca}_2\text{Si}_3\text{O}_9$ ), resulting in sintered specimens with increased remaining porosity. Bioactive glass sintering and the remaining micro-porosity can thus be tailored by variation of modifier type and glass particle size, allowing for flexibility in the design and preparation of porous bioactive glass scaffolds.


## ACKNOWLEDGMENTS

The authors thank I. Feldmann for electron microscopy investigations, D. Zwiazek and F. Kreidler for sample preparation and J. Brandt-Slowik and R. Wetzel for FTIR measurements.  $\mu\text{CT}$  experiments were performed on the I13-2 beamline of the Diamond Manchester Imaging Branchline at the Diamond Light Source synchrotron, Harwell, Didcot, Oxfordshire, UK; beamtime MT17001. We would like to acknowledge Mr Ligorio, Mr Naven, Mr McDowell, Ms Imere as well as staff at the Diamond Light Source, in

particular Dr A. Bodey for their contributions during the beamtime. Raw data requests are encouraged, for analysis and modelling applications, please contact Dr Gowsihan Poologasundarampillai at [g.poologasundarampillai@bham.ac.uk](mailto:g.poologasundarampillai@bham.ac.uk). Dr Poologasundarampillai acknowledges EPSRC grant EP/M023877/1.

## ORCID

Carsten Blaeß  <https://orcid.org/0000-0001-5620-2005>

Gowsihan Poologasundarampillai  <https://orcid.org/0000-0002-8498-323X>

Delia S. Brauer  <https://orcid.org/0000-0001-5062-0695>

## REFERENCES

- Hench LL, Splinter RJ, Allen WC, Greenlee TK. Bonding mechanisms at the interface of ceramic prosthetic materials. *J Biomed Mater Res.* 1971;5(6):117–41.
- Hench LL, Hench JW, Greenspan DC. Bioglass<sup>®</sup>: a short history and bibliography. *J Aust Ceram Soc.* 2004;40(1):1–42.
- Hench LL, Polak JM, Xynos ID, Buttery L. Bioactive materials to control cell cycle. *Mat Res Innov.* 2000;3(6):313–23.
- Xynos ID, Edgar AJ, Buttery L, Hench LL, Polak JM. Ionic products of bioactive glass dissolution increase proliferation of human osteoblasts and induce insulin-like growth factor II mRNA expression and protein synthesis. *Biochem Bioph Res Co.* 2000;276(2):461–5.
- Xynos ID, Hukkanen M, Batten JJ, Buttery LD, Hench LL, Polak JM. Bioglass<sup>®</sup> 45S5 stimulates osteoblast turnover and enhances bone formation in vitro: implications and applications for bone tissue engineering. *Calcified Tissue Int.* 2000;67(4):321–9.
- Jones JR, Brauer DS, Hupa L, Greenspan DC. Bioglass and bioactive glasses and their impact on healthcare. *Int J Appl Glass Sci.* 2016;7(4):423–34.
- Gomez-Vega JM, Saiz E, Tomsia AP, Oku T, Suganuma K, Marshall GW, et al. Novel bioactive functionally graded coatings on Ti6Al4V. *Adv Mater.* 2000;12(12):894–8.
- Lotfibakhshaiesh N, Brauer DS, Hill RG. Bioactive glass engineered coatings for Ti6Al4V alloys: influence of strontium substitution for calcium on sintering behaviour. *J Non-Cryst Solids.* 2010;356(44–49):2583–90.
- Meszáros R, Zhao R, Travitzky N, Fey T, Greil P, Wondraczek L. Three-dimensional printing of a bioactive glass. *Glass Technol.* 2011;52(4):111–6.
- Fu Q, Saiz E, Rahaman MN, Tomsia AP. Bioactive glass scaffolds for bone tissue engineering: state of the art and future perspectives. *Mat Sci Eng C-Mater.* 2011;31(7):1245–56.
- Pedone A, Charpentier T, Malavasi G, Menziani MC. New insights into the atomic structure of 45S5 bioglass by means of solid-state NMR spectroscopy and accurate first-principles simulations. *Chem Mater.* 2010;22(19):5644–52.
- Hill RG, Brauer DS. Predicting the bioactivity of glasses using the network connectivity or split network models. *J Non-Cryst Solids.* 2011;357(24):3884–7.
- Jones JR. Review of bioactive glass: from Hench to hybrids. *Acta Biomater.* 2013;9(1):4457–86.

14. Groh D, Döhler F, Brauer DS. Bioactive glasses with improved processing. Part 1. Thermal properties, ion release and apatite formation. *Acta Biomater.* 2014;10(10):4465–73.
15. Rau C, Wagner U, Pešić Z, De Fanis A. Coherent imaging at the Diamond beamline I13. *Phys Status Solidi A.* 2011;208(11):2522–5.
16. Pešić Z, De Fanis A, Wagner U, Rau C. Experimental stations at I13 beamline at Diamond Light Source. *J Phys Conf Ser.* 2013;425(18):182003.
17. Kak AC, Slaney M. Algorithms for reconstruction with nondiffracting sources. In: O'Malley RE, ed. *Principles of Computerized Tomographic Imaging.* Philadelphia, PA: Society for Industrial and Applied Mathematics; 2001.
18. Atwood RC, Bodey AJ, Price S, Basham M, Drakopoulos M. A high-throughput system for high-quality tomographic reconstruction of large datasets at Diamond Light Source. *Philos T R Soc A.* 2015;373(2043):20140398.
19. Strotton MC, Bodey AJ, Wanelik K, Darrow MC, Medina E, Hobbs C, et al. Optimising complementary soft tissue synchrotron X-ray microtomography for reversibly-stained central nervous system samples. *Sci Rep.* 2018;8:12017.
20. Schindelin J, Arganda-Carreras I, Frise E, Kaynig V, Longair M, Pietzsch T, et al. Fiji: an open-source platform for biological-image analysis. *Nat Methods.* 2012;9:676–82.
21. Arstila H, Tukiainen M, Taipale S, Kellomäki M, Hupa L. Liquidus temperatures of bioactive glasses. In: Liška M, Galusek D, Klement R, Petrušková V, ed. *Glass—The challenge for the 21st century.* Advanced materials research. Vol. 39–40. Stafa-Zurich, Switzerland: Trans Tech Publications; 2008:287–92.
22. Arstila H, Hupa L, Karlsson KH, Hupa M. Influence of heat treatment on crystallization of bioactive glasses. *J Non-Cryst Solids.* 2008;354(2–9):722–8.
23. Cable M. Classical glass technology. In: Zarzycki J, ed. *Glasses and amorphous materials.* Materials science and technology. A comprehensive treatment. Weinheim, Germany and New York, NY: VCH; 1991.
24. Brink M. The influence of alkali and alkaline earths on the working range for bioactive glasses. *J Biomed Mater Res.* 1997;36(1):109–17.
25. Watts SJ, O'Donnell MD, Law RV, Hill RG. Influence of magnesia on the structure and properties of bioactive glasses. *J Non-Cryst Solids.* 2010;356(9–10):517–24.
26. Tylkowski M, Brauer DS. Mixed alkali effects in Bioglass® 45S5. *J Non-Cryst Solids.* 2013;376:175–81.
27. Fagerlund S, Massera J, Hupa M, Hupa L. T-T behaviour of bioactive glasses 1–98 and 13–93. *J Eur Ceram Soc.* 2012;32(11):2731–8.
28. Fu Q, Rahaman MN, Bal BS, Brown RF, Day DE. Mechanical and in vitro performance of 13–93 bioactive glass scaffolds prepared by a polymer foam replication technique. *Acta Biomater.* 2008;4(6):1854–64.
29. Liu X, Rahaman MN, Fu Q, Tomsia AP. Porous and strong bioactive glass (13–93) scaffolds prepared by unidirectional freezing of camphene-based suspensions. *Acta Biomater.* 2012;8(1):415–23.
30. Pirhonen E, Niiranen H, Niemela T, Brink M, Tormala P. Manufacturing, mechanical characterization, and in vitro performance of bioactive glass 13–93 fibers. *J Biomed Mater Res B.* 2006;77B(2):227–33.
31. Brink M, Söderling E, Turunen T, Karlsson KH. Protein adsorption properties of bioactive glasses compared to their behavior in rabbit tibia. In: Wilson J, Hench LL, Greenspan D, eds. *Bioceramics 8.* Oxford, UK: Elsevier; 1995.
32. Brink M, Turunen T, Happonen RP, Yli-Urpo A. Compositional dependence of bioactivity of glasses in the system Na<sub>2</sub>O-K<sub>2</sub>O-MgO-CaO-B<sub>2</sub>O<sub>3</sub>-P<sub>2</sub>O<sub>5</sub>-SiO<sub>2</sub>. *J Biomed Mater Res.* 1997;37(1):114–21.
33. Bretcanu O, Chatzistavrou X, Paraskevopoulos K, Conradt R, Thompson I, Boccaccini AR. Sintering and crystallisation of 45S5 Bioglass® powder. *J Eur Ceram Soc.* 2009;29(16):3299–306.
34. Massera J, Fagerlund S, Hupa L, Hupa M. Crystallization mechanism of the bioactive glasses 45S5 and S53P4. *J Am Ceram Soc.* 2012;95(2):607–13.
35. Golovchak R, Thapar P, Ingram A, Savytskii D, Jain H. Influence of phase separation on the devitrification of 45S5 Bioglass. *Acta Biomater.* 2014;10(11):4878–86.
36. Prado MO, Zanotto ED. Glass sintering with concurrent crystallization. *Cr Chim.* 2002;5(11):773–86.
37. Döhler F, Groh D, Chiba S, Bierlich J, Kobelke J, Brauer DS. Bioactive glasses with improved processing. Part 2. Viscosity and fibre drawing. *J Non-Cryst Solids.* 2016;432:130–6.
38. Boccaccini AR, Chen Q, Lefebvre L, Gremillard L, Chevalier J. Sintering, crystallisation and biodegradation behaviour of Bioglass®-derived glass-ceramics. *Faraday Discuss.* 2007;136:27–44.
39. Clupper DC, Hench LL. Crystallization kinetics of tape cast bioactive glass 45S5. *J Non-Cryst Solids.* 2003;318(1–2):43–8.
40. Guillon O, Cao SY, Chang JY, Wondraczek L, Boccaccini AR. Effect of uniaxial load on the sintering behaviour of 45S5 Bioglass® powder compacts. *J Eur Ceram Soc.* 2011;31(6):999–1007.
41. Filgueiras MR, La Torre G, Hench LL. Solution effects on the surface reactions of a bioactive glass. *J Biomed Mater Res.* 1993;27(4):445–53.
42. Lusvardi G, Malavasi G, Cortada M, Menabue L, Menziani MC, Pedone A, et al. Elucidation of the structural role of fluorine in potentially bioactive glasses by experimental and computational investigation. *J Phys Chem B.* 2008;112(40):12730–9.
43. Brauer DS, Hill RG, O'Donnell MD. Crystallisation of fluoride-containing bioactive glasses. *Phys Chem Glasses.* 2012;53(2):27–30.
44. Ohsato H, Maki I, Takeuchi Y. Structure of Na<sub>2</sub>CaSi<sub>2</sub>O<sub>6</sub>. *Acta Crystallogr C.* 1985;41(NOV):1575–7.
45. Ohsato H, Takeuchi Y, Maki I. Structure of Na<sub>4</sub>Ca<sub>4</sub>[Si<sub>6</sub>O<sub>18</sub>]. *Acta Crystallogr C.* 1986;42:934–7.
46. Chen X, Hill R, Karpukhina N. Chlorapatite glass-ceramics. *Int J Appl Glass Sci.* 2014;5(3):207–16.
47. Wallace KE, Hill RG, Pembroke JT, Brown CJ, Hatton PV. Influence of sodium oxide content on bioactive glass properties. *J Mater Sci-Mater M.* 1999;10(12):697–701.
48. Arstila H, Vedel E, Hupa L, Hupa M. Factors affecting crystallization of bioactive glasses. *J Eur Ceram Soc.* 2007;27(2–3):1543–6.
49. Vedel E, Arstila H, Zhang D, Hupa L, Hupa M. Control of the forming properties of bioactive glasses. *Glass Technol.* 2007;48(4):191–5.
50. Wu ZY, Hill RG, Yue S, Nightingale D, Lee PD, Jones JR. Melt-derived bioactive glass scaffolds produced by a gel-cast foaming technique. *Acta Biomater.* 2011;7(4):1807–16.
51. Nommeots-Nomm A, Labbaf S, Devlin A, Todd N, Geng H, Solanki AK, et al. Highly degradable porous melt-derived bioactive glass foam scaffolds for bone regeneration. *Acta Biomater.* 2017;57:449–61.

52. Elgayar I, Aliev AE, Boccaccini AR, Hill RG. Structural analysis of bioactive glasses. *J Non-Cryst Solids*. 2005;351(2):173–83.
53. Pelton AD, Wu P. Thermodynamic modeling in glass-forming melts. *J Non-Cryst Solids*. 1999;253:178–91.
54. Brauer DS, Karpukhina N, Law RV, Hill RG. Structure of fluoride-containing bioactive glasses. *J Mater Chem*. 2009;19(31):5629–36.
55. O'Donnell MD, Watts SJ, Law RV, Hill RG. Effect of P<sub>2</sub>O<sub>5</sub> content in two series of soda lime phosphosilicate glasses on structure and properties—part II: physical properties. *J Non-Cryst Solids*. 2008;354(30):3561–6.
56. Brauer DS, Mneimne M, Hill RG. Fluoride-containing bioactive glasses: fluoride loss during melting and ion release in tris buffer solution. *J Non-Cryst Solids*. 2011;357(18):3328–33.
57. Brauer DS, Al-Noaman A, Hill RG, Doweidar H. Density-structure correlations in fluoride-containing bioactive glasses. *Mater Chem Phys*. 2011;130(1–2):121–5.
58. Christie JK, Pedone A, Menziani MC, Tilocca A. Fluorine environment in bioactive glasses: ab initio molecular dynamics simulations. *J Phys Chem B*. 2011;115(9):2038–45.
59. Christie JK, Brauer DS. The role of fluoride in the nanoheterogeneity of bioactive glasses. *Phys Chem Glasses*. 2017;58(4):180–6.
60. Frenkel J. Viscous flow of crystalline bodies under the action of surface tension. *J Phys (Moscow)*. 1945;9:385–91.
61. Arstila H, Fröberg A, Hupa L, Vedel E, Ylänen H, Hupa M. The sintering range of porous bioactive glasses. *Glass Technol*. 2005;46(2):138–41.
62. Müller R, Reinsch S. Viscous phase silicate processing. In: Bansal N, Boccaccini AR, ed. *Ceramics and composites processing methods*. Hoboken, NJ: John Wiley & Sons, Inc.; 2012:75–144.
63. Müller R. On the kinetics of sintering and crystallization of glass powders. *Glastech Ber-Glass Sci Technol*. 1994;67C:93–8.
64. Aguilar-Reyes EA, Leon-Patino CA, Jacinto-Diaz B, Lefebvre LP. Structural characterization and mechanical evaluation of bioactive glass 45S5 foams obtained by a powder technology approach. *J Am Ceram Soc*. 2012;95(12):3776–80.
65. Lefebvre L, Chevalier J, Gremillard L, Zenati R, Thollet G, Bernache-Assolant D, et al. Structural transformations of bioactive glass 45S5 with thermal treatments. *Acta Mater*. 2007;55(10):3305–13.
66. Adell V, Cheeseman CR, Doel A, Beattie A, Boccaccini AR. Comparison of rapid and slow sintered pulverised fuel ash. *Fuel*. 2008;87(2):187–95.
67. Müller R. The influence of grain-size on the overall kinetics of surface-induced glass crystallization. *J Therm Anal Calorim*. 1989;35(3):823–35.
68. Reis R, Zanotto ED. Simple model for particle phase transformation kinetics. *Acta Mater*. 2018;154:228–36.
69. Nommeots-Nomm A, Lee PD, Jones JR. Direct ink writing of highly bioactive glasses. *J Eur Ceram Soc*. 2018;38(3):837–44.

**How to cite this article:** Blaeß C, Müller R, Poologasundarampillai G, Brauer DS. Sintering and concomitant crystallization of bioactive glasses. *Int J Appl Glass Sci*. 2019;00:1–14. <https://doi.org/10.1111/ijag.13477>